Shock Waves (2006) 15(1(: 21–29
DOI 10.1007/s00193-005-0002-1

ORIGINAL ARTICLE

M. B. Liu · G. R. Liu · K. Y. Lam

Adaptive smoothed particle hydrodynamics for high strain hydrodynamics with material strength

Received: 29 July 2004 / Accepted: 1 July 2005 / Published online: 28 January 2006

Abstract This paper presents the implementation of an adaptive smoothed particle hydrodynamics (ASPH) method for high strain Lagrangian hydrodynamics with material strength. In ASPH, the isotropic kernel in the standard SPH is replaced with an anisotropic kernel whose axes evolve automatically to follow the mean particle spacing as it varies in time, space, and direction around each particle. Except for the features inherited from the standard SPH, ASPH can capture dimension-dependent features such as anisotropic deformations with a more generalized elliptical or ellipsoidal influence domain. Two numerical examples, the impact of a plate against a rigid surface and the penetration of a cylinder through a plate, are investigated using both SPH and ASPH. The comparative studies show that ASPH has better accuracy than the standard SPH when being used for high strain hydrodynamic problems with inherent anisotropic deformations.

Keywords Smoothed particle hydrodynamics · Adaptive smoothed particle hydrodynamics · Isotropic kernel · Anisotropic kernel · High strain hydrodynamics

PACS 46.15.-x, 83.10.Rs, 83.50.-v

1 Introduction

High strain hydrodynamics is generally characterized by the presence of shock waves, intense localized materials response, and impulsive loadings. Numerical simulation of high strain hydrodynamics with material strength such as high velocity impact (HVI) and penetrations is one of the formidable but attractive tasks in computational solid mechanics. Most of the wave propagation hydro-codes use traditional grid-based methods such as finite difference methods (FDM) and finite element methods (FEM) to simulate high strain hydrodynamics. Some of them are associated with advanced features, which attempt to combine the best advantages of FDM and FEM. Examples include arbitrary Lagrange–Eulerian (ALE) coupling and coupling Eulerian–Lagrangian (CEL). Though many successful achievements have been made using these methods, some numerical difficulties still exist. These numerical difficulties generally arise from large deformations, large inhomogeneities, and moving interfaces, free, or movable boundaries [1–6].

Recently growing interest has been focused on meshless methods, which are regarded as alternatives for the traditional grid-based numerical methods to simulate high strain hydrodynamics with material strength [7, 8]. Among the meshless methods, smoothed particle hydrodynamics (SPH) method [9, 10] is unique due to its special features as a meshless, particle-oriented method with pure Lagrangian nature. Since its invention to solve astrophysical problems in three-dimensional open space, SPH has been extensively studied and widely applied to different problems [11–14]. Libersky and his co-workers carried out the pioneering work of applying the SPH method to high strain hydrodynamic problems including HVI, fracture, and fragmentation [12, 15]. Johnson et al. [16, 17] proposed a normalized smoothing function (NSF) for axisymmetric problems based on the condition of uniform strain rate in the application of SPH to impact problems. Attaway et al. worked in coupling the SPH processor with a transient-dynamics FEM code, PRONTO, in which high strain areas that typically tangle or break conventional finite element meshes were resolved using the SPH method [18, 19].

The standard SPH method uses an isotropic smoothing kernel, which is characterized by a scalar smoothing length. One of the problems associated with the standard SPH is that the isotropic kernel of SPH can be seriously mismatched to

Communicated by K. Takayama

M. B. Liu (✉) · K. Y. Lam
College of Engineering,
Nanyang Technological University,
50 Nanyang Avenue, Singapore 639798
E-mail: liumb@ntu.edu.sg

G. R. Liu
Department of Mechanical Engineering,
National University of Singapore,
10 Kent Ridge Crescent, Singapore 119260

the anisotropic volume changes that generally occur in many problems. To closely match the anisotropic volume changes, an anisotropic smoothing kernel that can be characterized by a matrix (in a two-dimensional space) or a tensor (in a three-dimensional space) smoothing length can be efficacious. This leads to the development of the adaptive smoothed particle hydrodynamics (adaptive SPH or ASPH) in which the smoothing length can be adapted with the volume changes or other dimension-dependent features. The idea of using anisotropic kernel with SPH dates back to Bicknell and Gingold [20]. Shapiro et al. [21] first began investigating a generalized approach using an ellipsoidal kernel in SPH. Fulbright et al. [22] also presented a three-dimensional SPH designed to model systems dominated by deformation along a preferential axis using spheroidal kernels. Later Shapiro et al. [23] systematically introduced anisotropic kernels, tensor smoothing, and shock tracking to SPH to create ASPH. Owen et al. [24] presented an alternative formulation of the ASPH algorithm for evolving anisotropic smoothing kernels. Except for problems with anisotropic deformations, the concept of elliptical kernel has also been applied to channel flows with very large length width ratio for saving computational efforts [25]. The numerical results presented in the references further demonstrated that ASPH has better performance than the standard SPH in terms of resolving ability for a wide range of problems.

This paper presents the application of ASPH to simulating large strain hydrodynamics with material strength. The developed ASPH code is examined by two example problems, the impact of a plate against a rigid surface and the penetration of a cylinder through a plate. These two example problems are also investigated using the standard SPH method for comparison. The results obtained from numerical simulations are also compared with available experimental data, and data from other sources.

2 High strain hydrodynamics with material strength

The governing equations for high strain hydrodynamics with material strength are based on the conservation of mass, momentum, and energy as follows

$$\begin{cases} \dfrac{D\rho}{Dt} = -\rho \dfrac{\partial v^\beta}{\partial x^\beta} \\ \dfrac{Dv^\alpha}{Dt} = \dfrac{1}{\rho}\dfrac{\partial \sigma^{\alpha\beta}}{\partial x^\beta} \\ \dfrac{De}{Dt} = \dfrac{\sigma^{\alpha\beta}}{\rho}\dfrac{\partial v^\alpha}{\partial x^\beta} \\ \dfrac{Dx^\alpha}{Dt} = v^\alpha, \end{cases} \tag{1}$$

where the scalar density ρ, and internal energy e, the velocity component v^α, and the total stress tensor $\sigma^{\alpha\beta}$ are the dependent variables. The spatial coordinates x^α and time t are the independent variables. The summation in Eq. (1) is taken over repeated indices, while the total time derivatives are taken in the moving Lagrangian frame.

The total stress tensor $\sigma^{\alpha\beta}$ is made up of two parts, one part of isotropic pressure p and the other part of viscous shear stress τ

$$\sigma^{\alpha\beta} = -p\delta^{\alpha\beta} + \tau^{\alpha\beta}. \tag{2}$$

The isotropic pressure can be obtained using an equation of state (EOS) which describes the relationship of pressure to density and energy. Examples of EOS for solids include Mie-Gruneisen EOS [26], Tillotson EOS [27], and other possible choices.

The second part of shear stress in Eq. (2) is related to the resistance of the material to the shear deformation. The constitutive model, in general, permits the stress to be a function of strain and strain rate. For the anisotropic shear stress, if the displacements are assumed to be small, the stress rate is proportional to the strain rate through the shear modulus.

$$\dot{\tau}^{\alpha\beta} = \eta\bar{\varepsilon}^{\alpha\beta} = \eta\left(\varepsilon^{\alpha\beta} - \frac{1}{3}\delta^{\alpha\beta}\varepsilon^{\gamma\gamma}\right), \tag{3}$$

where η is the shear modulus, $\dot{\tau}$ is stress rate, and $\varepsilon^{\alpha\beta}$ is the strain rate tensor defined as

$$\varepsilon^{\alpha\beta} = \frac{1}{2}\left(\frac{\partial v^\alpha}{\partial x^\beta} + \frac{\partial v^\beta}{\partial x^\alpha}\right), \tag{4}$$

where $\bar{\varepsilon}^{\alpha\beta}$ is the traceless part of $\varepsilon^{\alpha\beta}$.

In order to get the material frame independent strain rate, the Jaumann rate is adopted with the following constitutive equation as

$$\dot{\tau}^{\alpha\beta} - \tau^{\alpha\gamma}R^{\beta\gamma} - \tau^{\gamma\beta}R^{\alpha\gamma} = \eta\bar{\varepsilon}^{\alpha\beta}, \tag{5}$$

where $R^{\beta\gamma}$ is the rotation rate tensor defined as

$$R^{\alpha\beta} = \frac{1}{2}\left(\frac{\partial v^\alpha}{\partial x^\beta} - \frac{\partial v^\beta}{\partial x^\alpha}\right). \tag{6}$$

The provisional von Mieses flow stress J is computed using the shear stress

$$J = \sqrt{\tau^{\alpha\beta}\tau^{\alpha\beta}}. \tag{7}$$

In the perfectly plastic yield model, the yield strength is constant if the second stress invariant J exceeds the known stress J_0. The shear stresses have to be scaled back to the yield surface

$$\tau^{\alpha\beta} = \tau^{\alpha\beta}\sqrt{J_0 3J^2}, \tag{8}$$

where J_0 is determined by the Johnson–Cook model, which describes the flow stress as a function of effective plastic strain, effective plastic strain rate, and temperature [28].

3 The standard SPH with isotropic kernels

In the SPH method, a set of arbitrarily distributed particles (points) is employed to represent the state of the system and record the movement of the system. Each particle is associated with physical parameters as mass, density, and pressure. The evolution of the system can be calculated based on the interaction of these particles and external forces. Specifically speaking, in the SPH method, a field function f and its first derivative at a particle i can be numerically approximated as the summation over the nearest neighboring particles through using a smoothing function (or kernel) W as follows:

$$\langle f\rangle_i = \sum_{j=1}^{N} (m_j/\rho_j) f_j W_{ij}, \tag{9}$$

$$\langle \nabla \cdot f\rangle_i = \sum_{j=1}^{N} (m_j/\rho_j) f_j \cdot \nabla_i W_{ij}, \tag{10}$$

where m_j and ρ_j are the mass and density of particle j. N is the total number of particles. Approximation of higher order derivatives can be carried out by nested approximations on lower order derivatives.

Figure 1 illustrates the standard SPH approximations with an isotropic kernel in a two-dimensional space. Only particles within the influence domain of the smoothing function W for particle i can contribute in the summation process. The influence domain of the isotropic kernel is circular with a radius of κh. V in Fig. 1 represents the problem domain with a surface S. The influence domain can be taken as any suitable shape. Different shapes of smoothing function can result in different versions or implementations of the SPH method. In the standard SPH method, the influence domain is usually taken as a circle (or a sphere in a three-dimensional space) with a scalar smoothing length h

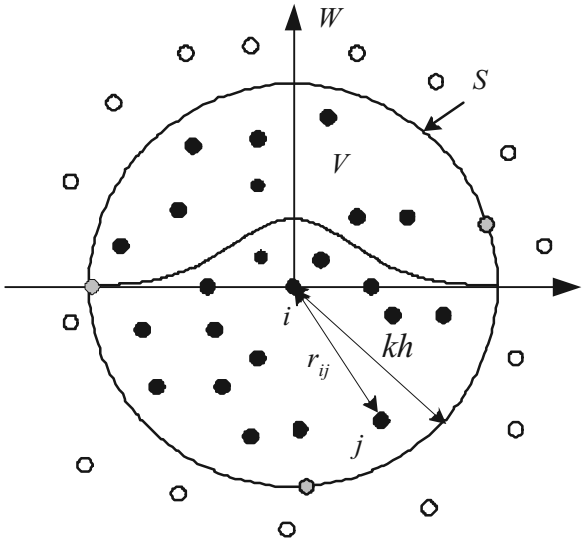

Fig. 1 SPH approximations with an isotropic kernel in a two-dimensional space

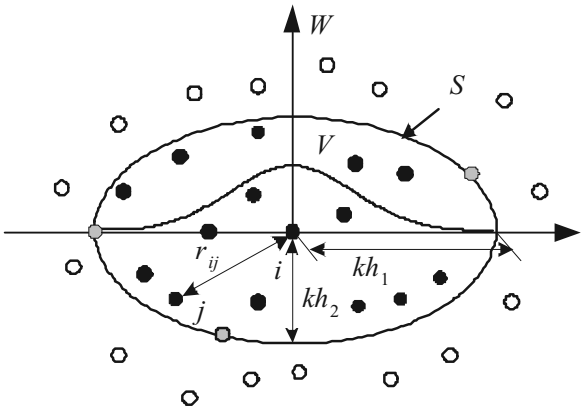

Fig. 2 ASPH approximations in a two-dimensional space. The influence domain of particle i is an ellipse rather than a circle in SPH

and a scaling factor κ. As will be discussed in the next section, the ASPH method employs an ellipsoidal smoothing function with a smoothing length tensor (Fig. 2).

In the standard SPH method with a spatially and temporally variable smoothing length, the scalar smoothing length h is usually adjusted according to the local density variation and it is in proportion to $\rho^{-1/d}$, where d is the number of dimensions. This is adequate for isotropic volume changes, but is seriously mismatched to the anisotropic volume changes. It is preferable to adjust the smoothing length to maintain a roughly constant number of neighbor particles and therefore to maintain the solution accuracy. One popular approach to evolve the smoothing length is [29]

$$\frac{dh}{dt} = -\frac{1}{d}\frac{h}{\rho}\frac{d\rho}{dt}. \tag{11}$$

One of the most widely used smoothing functions is the cubic spline devised by Monaghan and Lattanzio [30]. The cubic spline smoothing function and its first derivative are listed as follows

$$W(\kappa, h) = \alpha_d \times \begin{cases} \frac{2}{3} - \kappa^2 + \frac{1}{2}\kappa^3 & 0 \le \kappa < 1 \\ \frac{1}{6}(2-\kappa)^3 & 1 \le \kappa < 2 \\ 0 & \kappa \ge 2, \end{cases} \tag{12}$$

$$W'(\kappa, h) = \alpha_d \frac{1}{h}\frac{\bar{\kappa}}{\kappa} \begin{cases} -2\kappa + \frac{3}{2}\kappa^2 & 0 \le \kappa < 1 \\ -\frac{1}{2}(2-\kappa)^2 & 1 \le \kappa < 2 \\ 0 & \kappa \ge 2. \end{cases} \tag{13}$$

In Eq. (12) and (13), $\alpha_d = 1/h$, $15/7\pi h^2$, and $3/2\pi h^3$, respectively in one-dimensional, two-dimensional, and three-dimensional space. κ is the distance between two particles normalized by the scalar smoothing length h

$$\kappa = \frac{r}{h} = \frac{|\bar{r}|}{h} \quad \text{or} \quad \bar{\kappa} = \frac{\bar{r}}{h} = \frac{(x, y, z)}{h}, \tag{14}$$

where r is the real distance between two particles, $\bar{r}$ and $\bar{\kappa}$ are the real and normalized position vectors.

4 The ASPH with anisotropic kernel

The smoothing length determines the shape of the smoothing function and the pattern of interpolation and therefore it has direct influence on the efficiency of the computation and the accuracy of the solution. In general, the local mean interparticle spacing varies in time, space, as well as direction. The influence domain of the smoothing function should represent the variation of the interparticle spacing. The standard SPH method with a variable scalar smoothing length can only reflect the interparticle spacing variation in time and space. It does not show any feature of the directional effects. It can lose neighbor information in some directions and is not suitable for simulating problems with anisotropic deformations.

Based on such considerations, some models of adaptive smoothing particle hydrodynamics (ASPH) have been proposed to model the deformation in different directions [22, 24]. The ASPH models use an anisotropic algorithm that employs an ellipsoidal smoothing function characterized by a different smoothing length along each axis of the ellipsoidal. For two-dimensional cases, the influence domain of the smoothing function is elliptical (Fig. 2). The smoothing length along each axis is evolved so as to follow the variation of the local interparticle separation surrounding each particle. By deforming and rotating the ellipsoidal smoothing function so as to follow the anisotropic volume changes associated with each particle, ASPH adapts its spatial resolution scale in time, space, and direction. Hence, ASPH was shown to significantly improve the spatial resolving capability over that of the standard SPH method for the same number of particles used.

The main idea of the ASPH is that in three-dimensional space, the smoothing function is of ellipsoidal shape, which can be arbitrarily oriented. A smoothing tensor H can be used to characterize the influence domain of the smoothing function

$$H = \begin{pmatrix} h_{xx} & h_{yx} & h_{zx} \\ h_{xy} & h_{yy} & h_{zy} \\ h_{xz} & h_{yz} & h_{zz} \end{pmatrix}, \tag{15}$$

where $h_{yx} = h_{xy}$, $h_{zx} = h_{xz}$ and $h_{yz} = h_{zy}$. H is a second order, real and symmetric tensor. The eigenvectors of H are the directions along the three axes of the ellipsoid and the corresponding eigenvalues are the dimensions of the ellipsoid along each axis. SPH can be regarded as a special case of ASPH, with each diagonal element of H equal to h while other elements equal to zero. Therefore, one has more freedom with ellipsoidal smoothing functions than one has with spherical smoothing functions.

Similarly, the smoothing function in ASPH can be written as a function of the tensor smoothing length H and the normalized position vector $\bar{\kappa}$. In comparisons with SPH, the relation is as follows:

$$\begin{aligned} &\text{SPH:}\ \ \bar{\kappa} = \tfrac{1}{h}\bar{r}, \\ &\text{ASPH:}\ \ \bar{\kappa} = \tfrac{1}{H}\cdot\bar{r} = H^{-1}\cdot\bar{r} = G\cdot\bar{r}. \end{aligned} \tag{16}$$

The G tensor has units of the inverse of length. The cubic spline and its first derivative in ASPH can therefore be written as

$$W(\kappa, h) = \alpha_d \times \begin{cases} \frac{2}{3} - \kappa^2 + \frac{1}{2}\kappa^3 & 0 \le \kappa < 1 \\ \frac{1}{6}(2-\kappa)^3 & 1 \le \kappa < 2 \\ 0 & \kappa \ge 2, \end{cases} \tag{17}$$

$$W'(\kappa, h) = \alpha_d G \frac{\bar{\kappa}}{\kappa} \begin{cases} -2R + \frac{3}{2}\kappa^2 & 0 \le \kappa < 1 \\ -\frac{1}{2}(2-\kappa)^2 & 1 \le \kappa < 2 \\ 0 & \kappa \ge 2, \end{cases} \tag{18}$$

where in one-dimensional, two-dimensional, and three-dimensional spaces, $\alpha_d = |G|$, $\frac{15}{7\pi}|G|$ and $\frac{3}{2\pi}|G|$. The H or G tensor can be evolved both spatially and temporally. Owen et al. [24] gave an expressions for evolving the G tensor based on Eq. (11). The anisotropic volume changes represented by a smoothing ellipsoid can be transformed through a local, linear transformation of coordinates into those in which the underling anisotropic volume changes appear to be isotropic. For the kernel and particle approximation, as long as the quantities are expressed in terms of the normalized position vector $\bar{\kappa}$ rather than the explicitly using h, the SPH and ASPH dynamic equations are identical.

The smoothing function in both SPH and ASPH needs to be symmetrized if the smoothing lengths for each particle are spatially different. The symmetrization techniques in SPH and ASPH are also similar [8, 11, 24].

5 Discretized equations of motion for high strain hydrodynamics

Considering the artificial viscosity effect Π_{ij} [11], a set of particle equations of motion for simulating high strain hydrodynamics can be can be summarized as follows

$$\begin{cases} \dfrac{D\rho_i}{Dt} = \displaystyle\sum_{j=1}^{N} m_j \left(v_i^\beta - v_j^\beta\right) \frac{\partial W_{ij}}{\partial x_i^\beta} \\ \dfrac{Dv_i^\alpha}{Dt} = -\displaystyle\sum_{j=1}^{N} m_j \left(\frac{\sigma_i^{\alpha\beta}}{\rho_i^2} + \frac{\sigma_j^{\alpha\beta}}{\rho_j^2} + \Pi_{ij}\right) \frac{\partial W_{ij}}{\partial x_i^\beta} \\ \dfrac{De_i}{Dt} = \dfrac{1}{2}\displaystyle\sum_{j=1}^{N} m_j \left(\frac{p_i}{\rho_i^2} + \frac{p_j}{\rho_j^2} + \Pi_{ij}\right)\left(v_i^\beta - v_j^\beta\right) \\ \qquad\qquad \times \dfrac{\partial W_{ij}}{\partial x_i^\beta} + \dfrac{1}{\rho_i}\tau_i^{\alpha\beta}\varepsilon_i^{\alpha\beta} \\ \dfrac{Dx_i^\alpha}{Dt} = v_i^\alpha. \end{cases} \tag{19}$$

Equation (19) can be integrated using some standard methods such as Leapfrog method. The particle equations

for strain rate tensor and rotation rate tensor can be written as

$$\varepsilon_i^{\alpha\beta} = \frac{1}{2}\sum_{j=1}^{N}\frac{m_j}{\rho_j}\left[\left(v_j^\alpha - v_i^\alpha\right)\frac{\partial W_{ij}}{\partial x_i^\beta} + \left(v_j^\beta - v_i^\beta\right)\frac{\partial W_{ij}}{\partial x_i^\alpha}\right], \tag{20}$$

$$R_i^{\alpha\beta} = \frac{1}{2}\sum_{j=1}^{N}\frac{m_j}{\rho_j}\left[\left(v_j^\alpha - v_i^\alpha\right)\frac{\partial W_{ij}}{\partial x_i^\beta} - \left(v_j^\beta - v_i^\beta\right)\frac{\partial W_{ij}}{\partial x_i^\alpha}\right]. \tag{21}$$

6 Numerical examples

A series of numerical tests for simulating hydrodynamics with material strength were carried out using ASPH. The ASPH results were compared with the results obtained using the standard SPH method and other available experimental data as well as the data from other sources. Presented in this section are two typical cases. One is a cylinder impacting on rigid surface; another is a cylinder penetrating through on a plate. For these two examples, the coefficients for the linear and quadratic terms in the Monaghan-type artificial viscosity [11] were taken as unity, respectively.

6.1 A cylinder impacting on a rigid surface

In this example, an Armco iron cylinder (actually a plate in a two-dimensional space) traveling at 200 m/s impacted on a rigid surface. The plate was 2.546 cm long, and 0.760 cm wide. The motion was normal to the rigid surface. Libersky and Petschek [15] also numerically simulated this example using the standard SPH method. In this work, the Armco iron plate was modeled as an elastic-perfectly plastic material. The Mie–Gruneisen equation of state was employed. The material properties of the Armco iron and the parameters for the Mie–Gruneisen equation of state were the same as those in [15].

Sixty-seven particles were initially distributed along the length and 20 particles along the diameter for both the SPH and ASPH simulations. The rigid surface was distributed using 19 layers of virtual particles mirrored on the other side of the rigid surface. There were a total of 1340 real particles and 380 ghost particles. The cylinder was initially in contact with the rigid surface. In the SPH simulation, the initial smoothing length was slightly bigger (1.2 times) than the initial particle spacing so that in each direction a certain particle can have 5 effective neighbor particles including itself. In the ASPH simulation, the G tensor field was smoothed every two time steps, while the initial h_1 and h_2 were equal to 1.2 times the initial particle spacing in each dimension.

It was observed that the SPH simulation reached the steady state when the material nearly stopped deforming after around 90 μs. Figure 3 shows the steady state particle distributions using SPH. There are voids formed around the centre of the plate near the impact end. In the steady state, the length and diameter of the cylinder were 20.90 mm and 19.31 mm, respectively.

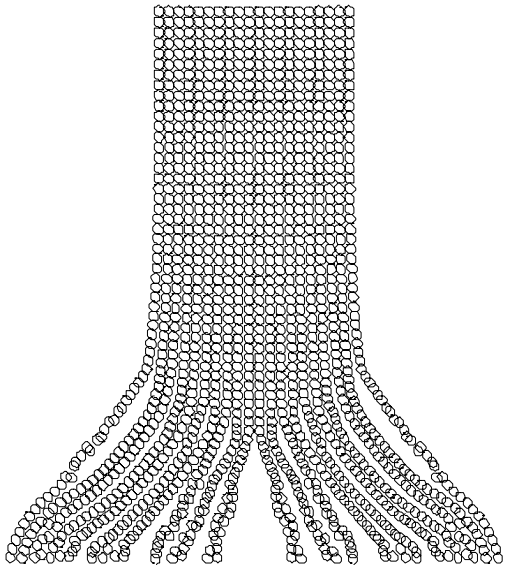

Fig. 3 Steady state particle distributions (after 90 μs) obtained using SPH for the example of a cylinder impacting on a rigid plate

Table 1 Final bar height and width from different sources

Real time (μs)	Final bar height (cm)	Final bar width (cm)
SPH results	2.09	1.93
ASPH results	2.14	1.62
Results by Libersky	2.18	1.52
Results by Johnson	2.11	1.70

The ASPH simulation also reached the steady state after around 90 μs. The length and diameter of the cylinder in the steady state were 21.36 cm and 16.16 cm, respectively. The particle distribution clearly shows that the particles are flattened along the direction of the impact. This obviously shows the anisotropy of the deformations. Different from the corresponding SPH plots, no void is formed around the centre of the plate near the impact end. This is an obvious advantage over the standard SPH method.

Table 1 shows the final bar height and width. The presented SPH and ASPH results were compared with the SPH results by Libersky and Petschek [15] and the results by Johnson using EPIC-2 [16, 17]. The final bar heights do not vary too much, but the final bar widths from different sources are quite different. The presented ASPH results show a good agreement with the results obtained by Johnson. Though the numerical accuracy needs to be guaranteed by convergence tests, the good agreement with the experiment justifies the numerical model. Detailed convergence study of ASPH is a subject of further works.

Table 2 Lapsed CPU time

Real time (μs)	SPH CPU time (s)	ASPH CPU time (s)
5	39.75	101.28
10	76.938	223.13
15	115.74	365.52
20	150.08	556.18
25	207.35	694.09
30	220.69	890.96
40	290.27	1249.3
50	365.02	1607.6
60	433.38	1804.8
70	506.23	2053.1
80	577.84	2275.7
100	712.54	2765.9

Table 2 shows the CPU time elapsed for both the SPH and ASPH simulations. The elapsed CPU times for the ASPH simulation were longer than those for the SPH simulation. There are some possible reasons. Firstly, in the ASPH simulation, the G tensor needs to be smoothed to stablize the numerical scheme every several steps. This smoothing process is quite time-consuming. Secondly, the anisotropy of the volume change leads to a compression of the smoothing length in some direction, which yields a smaller component of the smoothing length in that direction. The time step used in the integration is closely related to the smallest smoothing length component, and therefore becomes very small to be efficient.

6.2 HVI of a cylinder penetrating a plate

In this example, SPH and ASPH were applied to simulate the penetrating process of an infinitely long Al-cylinder through an infinitely long Al-plate. Since both the cylinder and the plate were infinitely long, the numerical simulation can be carried out on any middle section, therefore the problem can be simplified as a 2D problem. Hiermaier et al. [31] had done numerical simulations for this example in planar symmetry using their SPH code, SOPHIA. The cylinder was of 1.0 cm diameter. The plate was 0.4 cm thick. The plate length was of 10 cm. All particles were initialized as squares of 0.02 cm in side dimensions. The particles in the cylinder were arranged in circumferential rings as this gives a most realistic representation of the geometry. The particles in the plate were arranged in a rectangular Cartesian array (Fig. 5). There were 500 particles along the length and 20 particles along the thickness of the plate. There were 1956 particles in the cylinder and 10,000 particles in the plate, for a total of 11956 particles. The cylinder were initially in contact with the center of the plate.

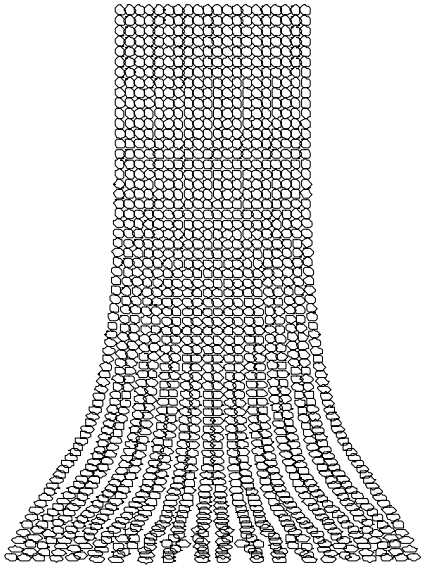

Fig. 4 Steady state particle distributions (after 90 μs) obtained using ASPH for the example of a cylinder impacting on a rigid plate

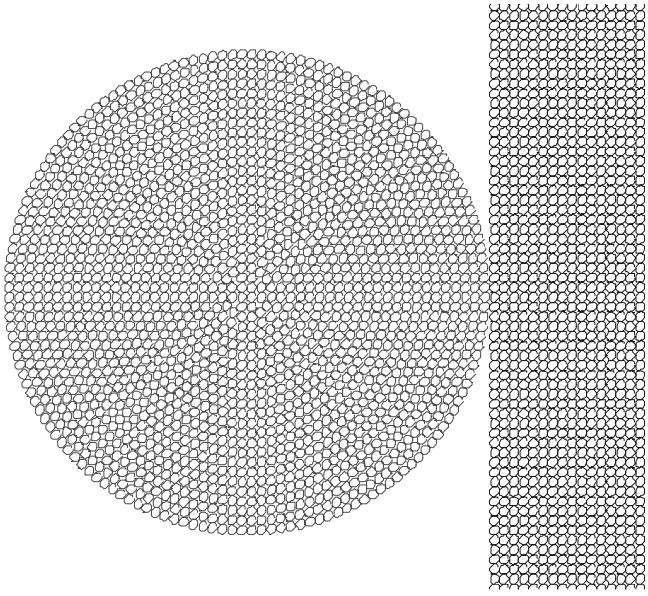

Fig. 5 Initial particle distribution in the vicinity of the contact area for both the SPH and ASPH simulation of a cylinder impacting on a plate. The particles near both ends of the plate were not plotted

The simulations were run to 20 μs. The impact speed of the cylinder was 6180 m/s. The Tillotson equation of state was used in this example. The material properties for aluminum can be found in Hiermaier et al. [31].

In the SPH simulation, the initial smoothing length was also set to be 1.2 times the particle spacing. Figure 6 shows the particle distributions obtained by the SPH simulation. The symmetry of the problem was well preserved. Figures 7 and 8 show the close-up view of the particles near the penetrated edge of the plate and the frontal region of the debris cloud, respectively. The outer layer of the debris cloud was made of the material from the plate, and the inner layer of the debris cloud was made up of the material from the cylinder.

In the ASPH simulation, the initial h_1 and h_2 were equal to 1.2 times the initial particle spacing in each dimension.

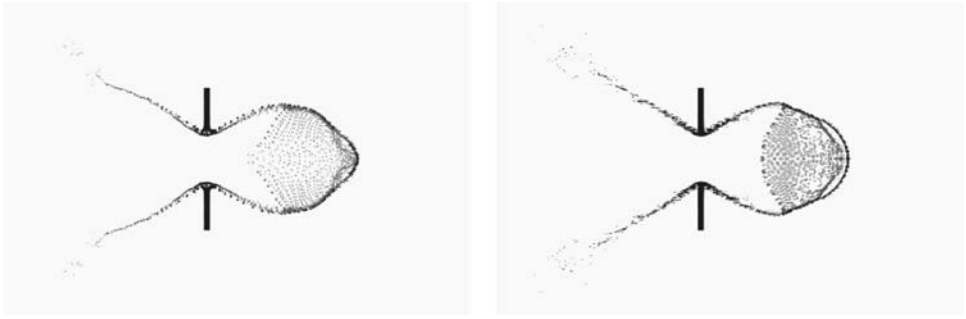

Fig. 6 Particle distributions at 20 μs obtained using SPH and ASPH for the example of an aluminium cylinder penetrating an aluminium plate

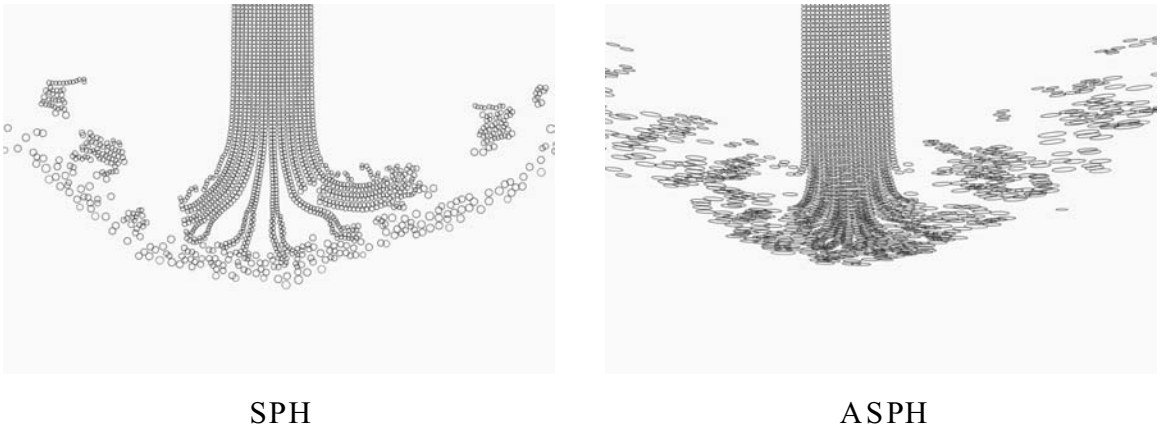

Fig. 7 Close-up view of the particle distributions at 20 μs near the penetrated edge of the plate for the example of an aluminium cylinder penetrating an aluminium plate

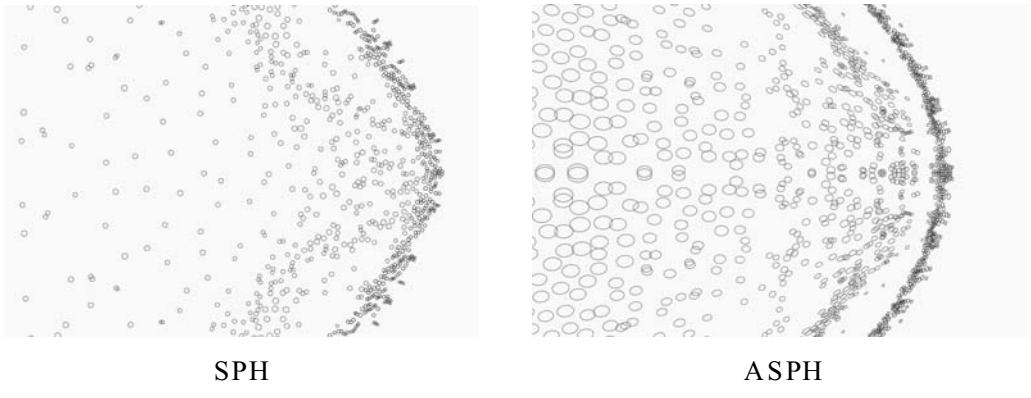

Fig. 8 Close-up view of the frontal region of the debris cloud at 20 μs

Figure 6 shows the particle distribution obtained by the ASPH simulation. Figures 7 and 8 show the close-up view of the particles near the penetrated edge of the plate and the frontal region of the debris cloud, respectively. In comparison with the SPH simulation, the orientation and anisotropy of the deformation of the particles can be clearly seen. This is an obvious advantage of using ASPH for HVI problems, which are associated with inherent anisotropic deformations. With changing orientation and anisotropy of volume, the ASPH method can give better predictions than SPH method.

Just as discussed in the above example, an obvious disadvantage of ASPH is that the computational expense of ASPH is much higher than that of SPH. Again, this is because in ASPH simulation, the anisotropic volume change leads to greatly reduced smoothing length in the compressed direction, which determines the time step used in the simulation.

Table 3 Comparison of crater diameters and shapes of the debris cloud [31]

	Experiment[a]	SPH[a]	ASPH	SPH
D_c (cm)	2.75–3.45	3.5	3.15	3.35
L/W	1.39	1.11	1.38	1.33

[a] The experimental data and SPH results were obtained from Hiermaier et al.

In order for the ASPH computation to reach the same interested time instant, it is necessary to take a larger number of smaller time steps.

The results of some key overall dimensions of the objects are shown in Table 3 together with the experimental data. In Table 3, D_c is the crate diameter, and L/W is the ratio of debris cloud length to debris cloud width. The experimental data was obtained from Hiermaier et al. [31], in which the crater diameter was given to be 2.75 cm when including crater lip, while 3.45 cm excluding crater lip. It should be noted that the experiment is a normal impact of a sphere on a plate, which is a three-dimensional axisymmetric problem. The numerical computations are all based on two-dimensional planar symmetric simulations. Hiermaier et al. [31] assumed that this is a probable cause of the discrepancies between their SPH simulation results and the experimental data. Except that, different SPH approximation schemes can lead to different numerical results, which can be closer to the experimental data. As shown in Table 3, the presented SPH and ASPH simulation results and the experimental data are in an acceptably agreement. The ASPH results, however, demonstrated much better accuracy.

7 Conclusion

High strain hydrodynamics characterized by the presence of strong shock waves, intense localized materials response, and impulsive loadings can usually lead to large deformation, which is generally anisotropic in different directions. The standard SPH method is associated with a scalar smoothing length, which can only reflect the interparticle spacing variation in time and space, but cannot show any feature of the directional effects. It can lose neighbor information in some directions and can have comparatively poorer accuracy for simulating high strain hydrodynamic problems with anisotropic deformations. ASPH replaces the isotropic kernel in the standard SPH with an anisotropic kernel whose axes evolve automatically to follow the mean particle spacing as it varies in time, space, and direction around each particle. It is a better choice to simulating high strain hydrodynamics with anisotropic deformations.

This paper presented the extension of ASPH to high strain Lagrangian hydrodynamics with material strength. Two numerical examples, the impact of a plate against a rigid surface, and the penetration of a cylinder through a plate, were investigated using both SPH and ASPH. It was demonstrated that ASPH has much better performance than the standard SPH in simulating high strain hydrodynamics. ASPH can capture dimension-dependent features such as anisotropic deformations. ASPH, however, suffers from bigger computational expense than the standard SPH.

Acknowledgements The authors would like to acknowledge the previous work made by Mr. G. L. Chin.

References

1. Benson, D.J.: Computational methods in Lagrangian and Eulerian hydrocodes. Comput. Methods Appl. Mech. Eng. **99**, 235–394 (1992)
2. Charles, E.A. Jr.: An overview of the theory of hydrocodes. Int. J. Impact Eng. **5**, 33–59 (1987)
3. Hans, U.M.: Review: hydrocodes for structure response to underwater explosions. Shock Vib. **6**(2), 81–96 (1999)
4. Liberskty, L.D., Petschek, A.G., Carney, T.C., Hipp, J.R., Allahdadi, F.A.: High strain Lagrangian hydrodynamics. J. Comput. Phys. **109**, 67–75 (1993)
5. Swegle, J.W., Attaway, S.W.: On the feasibility of using smoothed particle hydrodynamics for underwater explosion calculations. Comput. Mech. **17**, 151–168 (1995)
6. Walters, W.P., Zukas, J.A.: Fundamentals of shaped charges. Wiley (1989)
7. Liu, G.R.: Mesh free methods: moving beyond the finite element method. CRC Press, Boca Raton, FL (2002)
8. Liu, G.R., Liu, M.B.: Smoothed particle hydrodynamics—a meshfree particle method, World Scientific, Singapore (2003)
9. Lucy, L.: A numerical approach to testing the fission hypothesis. Astron. J. **82**, 1013–1024 (1977)
10. Gingold, R.A., Monaghan, J.J. Smoothed particle hydrodynamics: theory and application to non-spherical stars. Mon. Not. R. Astron. Soc. **181**, 375–389 (1977)
11. Monaghan, J.J.: Smoothed particle hydrodynamics. Annu. Rev. Astron. Astrophys. **30**, 543–574 (1992)
12. Randles, P.W., Libersky, L.D. Smoothed particle hydrodynamics: some recent improvements and applications. Comput. Methods Appl. Mech. Eng. **139**, 375–408 (1996)
13. Liu, M.B., Liu, G.R., Zong, Z., Lam, K.Y.: Computer simulation of the high explosive explosion using smoothed particle hydrodynamics methodology. Comput. Fluids **32**(3), 305–322 (2003a)
14. Liu, M.B., Liu, G.R., Zong, Z., Lam, K.Y.: Smoothed particle hydrodynamics for numerical simulation of underwater explosions. Comput. Mech. **30**(2), 106–118 (2003b)
15. Libersky, L.D., Petscheck, A.G.: Smoothed particle hydrodynamics with strength of materials, In: Proceedings of The Next Free Lagrange Conference, Springer-Verlag, New York, pp. 248–257 (1991)
16. Johnson, G.R., Petersen, E.H., Stryk, R.A.: Incorporation of an SPH option into the EPIC code for a wide range of high velocity impact computations. Int. J. Impact Eng. **14**, 385–394 (1993)
17. Johnson, G.R., Stryk, R.A., Beissel, S.R.: SPH for high velocity impact computations, Comput. Methods Appl. Mech. Eng. **139**, 347–373 (1996)
18. Plimpton, S.J., Attaway, S., Hendrickson, B., Swegle, J., Vaughan, C., Gardner, D.: Parallel transient dynamics simulations: algorithms for contact detection and smoothed particle hydrodynamics. J. Parallel Distr. Commun. **50**, 104–122 (1998)
19. Brown, K., Attaway, S., Plimpton, S.J., Hendrickson, B.: Parallel strategies for crash and impact simulations, Comput. Methods Appl. Mech. Eng. **184**, 375–390 (2000)
20. Bicknell, G.V., Gingold, R.A.: On tidal detonation of star by massive black holes. Astrophys. J. **273**, 749–760 (1983)

21. Shapiro, P.R., Martel, H., Villumsen, J.V., Kang, H.: Smoothed particle hydrodynamics and the simulation of galaxy and large-scale structure formation. Rev. Mexi. Astron. Astrofis. **27**, 187–190 (1993)
22. Fulbright, M.S., Benz, W.: A method of smoothed particle hydrodynamics using spheroid kernels. Astron. J. **440**, 254–262 (1995)
23. Shapiro, P.R., Martel, H., Villumsen, J.V., Owen, J.M.: Adaptive smoothed particle hydrodynamics, with application to cosmology: methodology. Astrophys. J. Suppl. S. **103**, 269–330 (1996)
24. Owen, J.M., Villumsen, J.V., Shapiro, P.R., Martel, H.: Adaptive smoothed particle hydrodynamics: methodology. II. Astrophys. J. Suppl. S. **116**, 155–209 (1998)
25. Liu, M.B., Liu, G.R.: Meshfree particle simulation of micro channel flows with surface tension. Comput. Mech. **35**, 332–341 (2005)
26. Zukas, J.A.: High velocity impact, Wiley, New York (1990)
27. Tillotson, J.H.: Metallic equations of state for hypervelocity impact. GA-3216, General Atomic, San Diego, CA (1962)
28. Johnson, G.R., Cook, W.H.: A constitutive model and data for metals subjected to large strains, high strain rates and high temperatures. In: Proceedings of the Seventh International Symposium on Ballistics, The Hague, The Netherlands, pp. 541–547 (1983)
29. Benz, W.: Smoothed particle hydrodynamics: a review. NATO Workshop, Les Arcs, France (1989)
30. Monaghan, J.J., Lattanzio, J.C.: A refined particle method for astrophysical problems. Astron. Astrophys. **149**, 135–143 (1985)
31. Hiermaier, S., Konke, D., Stilp, A.J., Thoma, K.: Computational simulation of the hypervelocity impact of Al-sphere on thin plates of different materials. Int. J. Impact Eng. **20**(1–5), 363–374 (1997)